T^{-n} (*n*: 2.4~2.56) temperature dependence of thermal resistance at single-walled carbon nanotubes/SiO$_2$ interface at <8 nm scale

Ibrahim Al Keyyam [a], Mahya Rahbar [a], Nicholas Hunter [a], Baini Li [b], Tianyu Wang [b,*], Enzheng Shi [b], Xinwei Wang [a,*]

[a] *Department of Mechanical Engineering, Iowa State University, Ames, IA 50011, USA*
[b] *Research Center for Industries of the Future, Key Laboratory of 3D Micro/Nano Fabrication and Characterization of Zhejiang Province, School of Engineering, Westlake University, Hangzhou, 310024, PR China*

ARTICLE INFO

ABSTRACT

The burgeoning significance of energy coupling at interfaces of nm dimension aligns seamlessly with the rapid strides made in micro/nanoelectronics. The nm-scale interface thermal resistance (ITR) is strongly affected by temperature but is poorly understood to date due to extreme challenges in nm-scale characterization. This work reports a pioneering and high-level study on how temperature affects the ITR of single-walled carbon nanotube (SWCNT)-SiO$_2$ interface with $a < 8$ nm lateral dimension. From 297 to 77 K, the ITR is observed to increase from 530 to 725 to $(1.56–1.74)\times10^4$ K·m·W^{-1}. The reported ITRs at room temperature are in line with reported data for SWCNT/SiO$_2$ interface. The ITR variation with temperature is compared with the prediction based on the phonon diffuse mismatch model (DMM). A great qualitative agreement is observed while the DMM under the Debye approximation of linear dispersion underestimates the ITR. Our ITR dependency on temperature takes the form of T^{-n} where *n* is found to be 2.4 and 2.56 for two different locations of the sample. Such observation resembles the dependency of specific heat on temperature far below the Debye temperature. We introduce a concept termed as the effective interface energy transmission velocity ($v_{i,eff}$) in an attempt to rule out the role of specific heat in ITR-temperature dependence to uncover the intrinsic effect of temperature on interface energy coupling. Very interestingly, $v_{i,eff}$ shows little variation over a wide temperature range for various reported interfaces. Further exploration and refinement of this concept is expected in forthcoming research endeavors.

1. Introduction

The exploration of interfacial thermal resistance (ITR) has undergone significant expansion and diversification [1]. This shift is primarily attributed to the rapid advancements in semiconductor and energy industries, particularly the miniaturization of microelectronics and the emergence of nanotechnology [2]. The relentless progress in microelectronic devices, characterized by enhanced speed and power, has amplified the significance and urgency of investigating ITR. Moreover, as semiconductor technology permeates various applications, the ITR challenge has surfaced in novel fields and devices, encompassing light-emitting diodes, quantum cascade lasers, phase change memory, thermoelectric devices, wearable devices, and photovoltaic cells. Additionally, the role of ITR in efficient heat dissipation from batteries is pivotal, as demonstrated in studies focused on smartphone and electric vehicle batteries. Inadequate heat removal from these energy storage systems not only compromises performance and reliability but also poses the risk of catastrophic consequences, including device failure and potential fire hazards [3].

For efficient microelectronics design, the underlying physics behind the ITR must be understood at the atomistic level. The conventional models of phonon transport at material interfaces, such as the acoustic mismatch model (AMM) [4] and diffuse mismatch model (DMM) [5], have primarily focused on the frequency mismatch between the two materials at the bulk scale. The surface roughness is yet another factor that impacts the conductance at the interface. We have demonstrated in our previous work that rough contact can enhance the thermal transport at the interface [6]. In fact, the surface roughness can act as a modifier that smoothens the transition from high to low acoustic impedance mediums in highly mismatched interfaces, thereby enhancing thermal energy transfer across the interface. The efficiency of heat transfer across interfaces is influenced by the nature of bonding between the

---

materials. For single-walled carbon nanotubes (SWCNT) on a silicon (Si) substrate, it has been observed that a covalently bonded interface exhibits a significantly lower interfacial thermal resistance compared to a van der Waals bonded interface [7]. This finding can be attributed to the higher density of low-frequency phonons, specifically the radial breathing mode, in the covalently bonded interface compared to the van der Waals bonded interface. The density of states of tangential modes, which correspond to high-frequency phonons around the G band, showed no significant difference, suggesting that longer wavelength phonons play a more prominent role in heat transfer. Additionally, it was observed that van der Waals forces between different nanotubes within the bundle enhance the interfacial thermal conductance [8].

Carbon nanotubes (CNTs) have captured the interest of many researchers [9], mainly for their exceptional thermophysical properties [10]. They have been proposed for various applications, from space elevators to thermal interface materials (TIM) between surfaces in contact [11]. Achieving perfect contact is practically impossible, and tiny air gaps will inevitably be present. These air gaps pose a challenge to efficient heat transfer, as the thermal conductivity of air (0.026 W·m^{-1}·K^{-1}) is approximately four orders of magnitude lower than that of metals. Consequently, hotspots can form within devices, reducing device efficiency and acting as a bottleneck for the advancement of microelectronics [12]. Harnessing the exceptional properties of CNTs, researchers have turned their attention to utilizing these one-dimensional structures as advanced TIMs. CNTs exhibit remarkable thermal conductivity, surpassing conventional TIM materials, and can efficiently bridge gaps between uneven surfaces, minimizing thermal contact resistance. Furthermore, their flexibility and compressibility enable conformal contact, optimizing heat transfer. Combining low density with outstanding chemical stability, CNT-based TIMs offer lightweight solutions that can withstand harsh environments and high temperatures [11, 13].

The solid-solid ITR have been studied extensively for different materials via computational models and various experimental techniques. The metal-metal interface is studied in details by Gundrum *et al.* [14] and is found to be one order of magnitude higher than a typical metal-dielectric interface. These results were compatible with the predicted by the DMM. The enhanced transport is well understood by the existence of free electrons in metals, which contributes significantly to heat transport [15]. Numerous studies experimentally have measured the ITR between CNTs and different substrates. The reported values vary, partly due to the different uncertainty levels introduced by different experimental techniques. For instance, Pop *et al.* [16] examined the electrical and thermal characteristics of metallic SWCNTs on insulating substrates using in-air joule breakdown of SWCNT. They determined the thermal conductance between SWCNTs and substrates to be 0.17 ± 0.03 W·m^{-1}·K^{-1}. Additionally, their findings indicated that electrons contribute less than 15 % to the overall thermal conductivity of metallic nanotubes at room temperature. Maune *et al.* reported the ITR between SWCNT and sapphire substrate of around 3 K·m·W^{-1} [17] utilizing electrical breakdown phenomenon. The results indicate that it suffices to have a contact length between SWCNT and solid substrates for an efficient heat transport, and the heat transport is dominated by interfacial resistance rather than the conduction resistance in the substrate. Shi *et al.* [18] reported the interfacial thermal conductance for SWCNT on SiO$_2$ to reach 0.7×10^{-4} W·m^{-1}·K^{-1}. Yang *et al.* measured the ITR between multi-walled carbon nanotubes (MWCNT) to be in the order of 10^{-9} K·m^2·W^{-1} [19]. They reported that as the contact area transitions from a cross-contact to an aligned contact, the thermal conductance at the interface can surge by almost two orders of magnitude. Yang *et al.* reported a cross-contact interfacial thermal conductance that ranges from 3×10^8–1.3×10^9 W·m^{-2}·K^{-1} for MWCNTs, where it is found to have a linear dependence on the tube diameter. In our recently published work [20], we reported the interfacial thermal conductance between nm-scale SWCNT bundle and Si to be in the range $(2.5$–$5.6) \times 10^{-4}$ W·m^{-1}·K^{-1}. The results suggest a loose contact with the

substrate possibly due to the nonuniformity of the bundle as revealed by atomic force microscopy (AFM) and Raman scanning.

The former studies give a comprehensive idea on the nature of the energy coupling at the interface between CNTs and different substrates at room temperature. However, they give little to no insight into how the interfacial thermal conductance varies with temperature. The impact of the temperature variation on the energy transport at the graphene/SiO$_2$ interface is studied by Chen *et al.* [1] using the 3ω method for different sample thicknesses. Their results indicate an inverse relation between the ITR and the temperature, with no clear thickness dependency. The room temperature ITR varies in a range of $(0.56$–$1.2) \times 10^{-8}$ K·m^2/W which is significantly lower than the reported values for carbon-based materials cited earlier. Wang *et al.* [21] have investigated the interfacial thermal conductance of mechanically exfoliated black phosphorus and SiO$_x$ for different thickness range. Their results confirm the thickness independency and suggest that the discrepancies of the interfacial thermal conductance from sample to sample overshadow the intrinsic thickness dependency. However, their ITR values show a direct proportionality with temperature, contrary to the expectations, yet are consistent with previous work reported by Taube *et al.* [22]. The reported ITR values in their research vary from $(0.88$–$4.6) \times 10^{-8}$ K·m^2/W. Despite its importance, no study was reported to address the impact of temperature on the energy coupling between SWCNTs and SiO$_2$ substrate, to our best knowledge. Hence, this study aims to bridge the gap for a better understanding of the underlying physics of the SWCNT/SiO$_2$ interface.

Here, we present a comprehensive investigation of the temperature dependent ITR for SWCNT bundle on a SiO$_2$ substrate. To the best of our knowledge, this is the first systematic exploration of the temperature dependency of the ITR at the SWCNT/SiO$_2$ interface. The outcomes of this research are expected to enhance our understanding of the underlying physics of the interface energy transport between SWCNTs and SiO$_2$ and are essential when temperature variation exists in many applications such as batteries and thermoelectrics. Nanosecond-resolved Raman thermal probing offers a significant advantage over traditional techniques when analyzing the thermal properties of carbon nanotubes and their interaction with substrates, particularly for the nanosized 1-dimensional (1D) contact between the SWCNT and the substrate. This allows for highly localized and sensitive measurements of thermal response, providing insights into the unique thermal transport mechanisms within these structures that are not accessible through conventional methods [23]. We employ an innovative technique developed in our lab, the energy transport state-resolved Raman (ET-Raman), which effectively mitigates the uncertainties associated with laser absorption measurements and Raman temperature calibration [24].

The temperature-dependent investigations are conducted by precisely controlling the sample's temperature using liquid nitrogen. We differentiate the thermal energy transport mechanisms in the SWCNT sample at each temperature point under laser heating. The differentiation is achieved by alternating between a continuous wave (CW) laser beam and an amplitude-modulated nanosecond pulsed beam, introducing a unique temperature rise exclusively within the SWCNT. Experimentally measurable Raman signal redshifts are effectively generated by analyzing the resulting Raman wavenumber with varied laser powers. The ET-Raman technique is designed to use the relative Raman wavenumber redshift information. Consequently, as discussed in previous work, it circumvents the need for a sample-dependent Raman temperature coefficient and mitigates the potential impact of light interference at the interfacial gap. We have developed a robust numerical model based on the finite-volume method, which solves the heat equation and extracts the ITR at each temperature. The forthcoming sections will expound in greater detail on the experimental methodology, the results of the temperature-dependent investigations, and the underlying physical insights gleaned from this research.

2. Sample structure characterization

SWCNTs used in this work are synthesized using atmospheric pressure chemical vapor deposition (APCVD) with sulfur, ferrocene, and xylene as initiator materials. The growth process involves placing a nickel foil downstream of a quartz tube in a CVD furnace. Initially, the furnace is heated to 1160 °C under a pure argon gas stream. A solution of sulfur and ferrocene dissolved in xylene is then injected into the upstream side of the quartz tube while simultaneously switching the carrier gas to a mixture of argon and hydrogen. The flow rates are controlled to achieve the desired conditions. The reaction time is varied to control the thickness of the CNT films. After growth, the CNT films are collected on the nickel foil and transferred onto a silicon substrate.

Atomic force microscopy (AFM) is first used to characterize the sample's profile as illustrated in Fig.1a, with the specific locations of interest marked in red dashed line. The AFM results revealed a reduction in the height of the bundle from 7.7 to 5.55 nm, at the first and second locations as shown in Fig. 1b and 1c, respectively. The shaded green areas in Fig. 1b and 1c illustrate the laser spots in Raman spectroscopy study. To study this variation, the radial breathing mode (RBM) peaks in the Raman spectra are acquired and analyzed. The RBM are commonly used to determine the diameter of individual SWCNTs within the bundle, where the frequency (ω_{RBM}) is known to be inversely proportional to the tube diameter (d) as $d = A/\omega_{RBM}$ where A is taken as 223.75 (cm^{-1} nm) [25].

Here, we utilize the RBM peaks as identified in Fig. 1e and 1f to calculate the diameter of the individual SWCNTs and reveal the

structure. We collect the RBM spectrum using 2400 grating/mm, allowing for a high spectral resolution. Thus, we account for the peaks as illustrated where any abrupt discontinuity is considered to represent a distinct peak. Using the previous relation, the diameter of each distinct SWCNT can be calculated based on the frequency of the peak. This has an impact on calculating the effective density of the SWCNT bundle, which is the density of graphite corrected by a factor $\gamma = A_s/A_c$ that represents the packing density of the SWCNT bundle. Here A_s is the solid area of the bundle and calculated as $A_s = \sum (\pi/4)(d_o^2 - d_i^2)$ and A_c is the total area enclosed by the AFM measurements. d_o is the diameter of individual SWCNTs as revealed by the RBM, $d_i = d_o - 2t$, and $t = 0.335$ nm as the SWCNT wall thickness [26]. Here we assume there exists only one individual SWCNT per RBM peak, which is reasonable for such a smaller diameter bundle. This yields the minimum packing density γ_{min} inside the bundle which is calculated to be 43 % and 50 % for the first and second locations. Consequently, it leads to the upper limit of the ITR (detailed in Section 4). The packing density is then maximized by allowing double counting of some RBM peaks such that the nominal area of the bundle as measured by the AFM is fully occupied, which yields γ_{max} to be 63 % for the two locations. We emphasize here that γ_{max} cannot exceed this value since individual SWCNT themselves are hollowed and hence there exist an inevitable porosity in the bundle that cannot be filled. Solving the heat equation under this condition yields a lower limit of ITR. In general, the ITR and the mass inside the bundle are related such that $\rho R'$ is an invariant where ρ is the density of the bundle and R' is the ITR. The results are shown in Fig. 4b and will be discussed in detail later. To calculate the nominal dimensions of the bundle, we note that
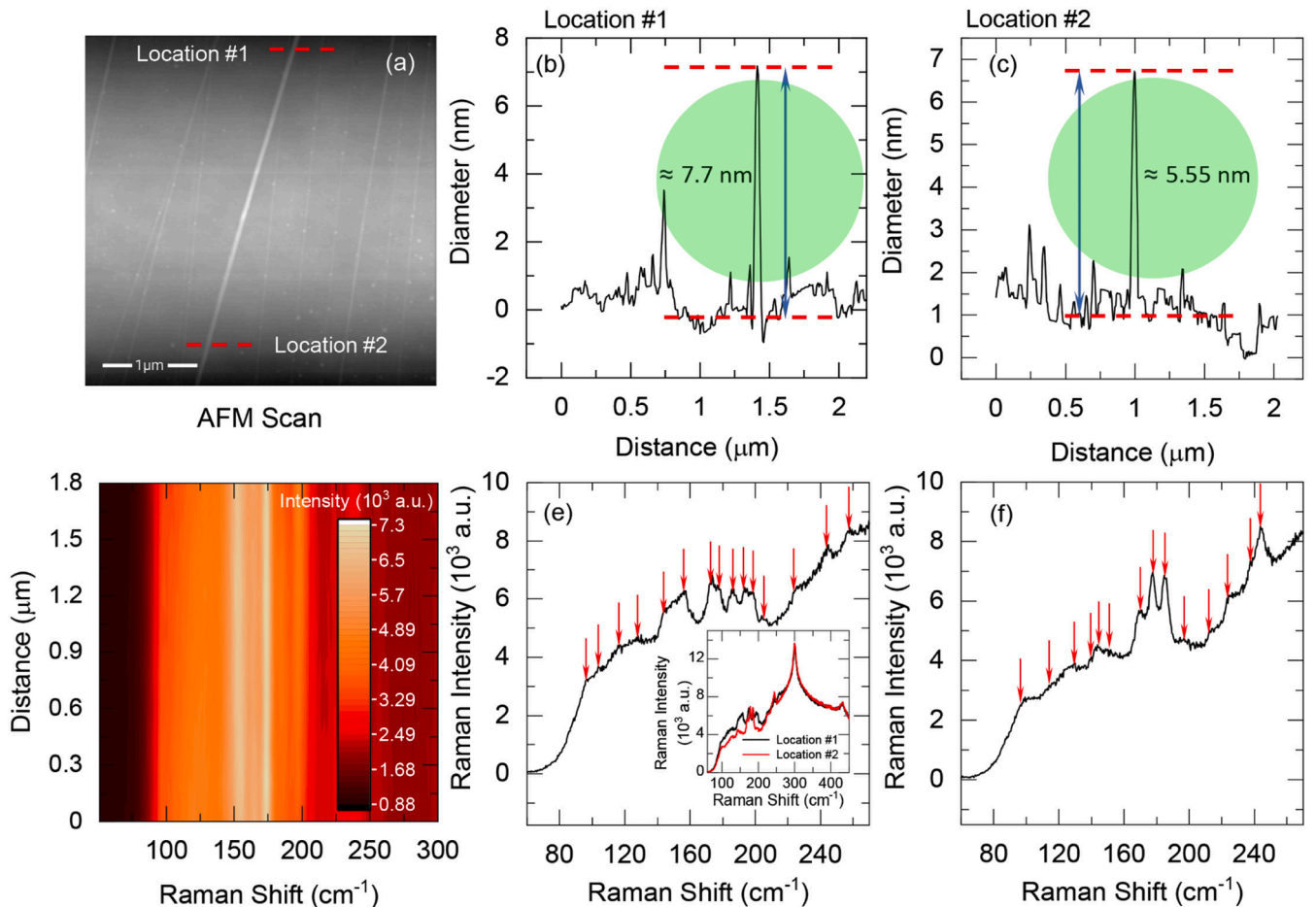

Fig. 1. (a) AFM scan image. Sample height measurement by AFM, with the laser spot size shown in the green shaded area for (b) Location #1 (c) Location #2. (d) Radial breathing modes (RBM) scan. RBM under the 532 nm laser excitation with identified peaks for (e) Location #1 (f) Location #2. The RBM of the two locations are compared in the inset of figure (e).

the AFM measurements usually provide confident probing of the sample's height, but it inevitably overestimates the width due to the tip convolution. The apparent width (w) as revealed by AFM measurements is 22.74 and 24.21 nm for the locations with heights of 7.7 and 5.55 nm. The AFM tip used in the measurement is circular and has a radius of 10 nm. The width measured by the AFM is a function of the AFM tip radius and the intrinsic radius of the sample, which can be approximated using $w \simeq 4(r_{tip} \cdot r_{sample})^{1/2}$ as widely adopted in literatures [27]. Consequently, the sample's width ($2r_{sample}$) after the correction is 6.5 and 7.3 nm for location #1 and #2.

3. Physics of ET-Raman and experimental procedure

Conventional Raman measurement for thermal characterization relies heavily on the Raman temperature coefficient. Not only this, but the laser absorption coefficient plays a vital role in estimating the absorbed laser energy. The ET-Raman is a novel technique that successfully eliminates such unnecessary dependency by establishing two distinct energy-transport states to characterize the ITR between the SWCNT bundle and the SiO$_2$ substrate (300 nm on Si wafer). A 50× objective lens focuses the laser onto the sample, with a laser spot size of ~ 1.5 μm as shown in the inset of Fig. 2. The steady-state heating employs a CW laser with a wavelength of 532 nm (photon energy of 2.33 eV). On the other hand, the transient state uses a function generator to modulate the CW laser and achieve a square-wave nanosecond pulse. The square-wave pulse's duty defined as $t_e/(t_e+t_r)$ is set to be 1.96 %, corresponding to 20 ns of laser heating time (t_e) and 1 μs relaxation time (t_r). The 1 μs off-time has been chosen to ensure the sample has enough time to cool down, yielding a more distinct energy transport state than the CW laser heating. If the material does not get enough time to thermally relax, a remnant of the heating effect might still exist in the sample before the new pulse comes in [26]. As a result, the temperature will start to build up and eventually reach the steady state scenario. The temperature profile of the sample under consideration, which may not necessarily correspond to its true temperature increase, can be obtained by acquiring the Raman spectrum. By comparing the response of a steady state heating using a CW laser to that of a transient response using an amplitude-modulated laser, we eliminate the necessity to calculate the Raman temperature coefficient of the sample, which carries its own uncertainties to the measurement. More thorough discussion can be found in our previous work [28].

In the experiment, the laser power (P) is tuned using an automated filter controlled by LabVIEW to facilitate the experimental procedure. The range of laser power is chosen to obtain a sound Raman spectrum

and an observed redshift while simultaneously ensuring the sample is undamaged. The Raman spectrum is collected at each laser power using *HORIBA-iHR550* spectrometer. The G band, which is a first-order Raman active mode of SWCNTs represented by a dominant peak around 1586 cm^{-1} in the Raman spectrum, is chosen for the analysis due to its optimal signal-to-noise ratio. The G band wavenumber is identified by employing a Gaussian fitting to the Raman spectrum. Once the Raman spectrum is collected, we plot the wavenumber variation with the laser power to obtain the Raman shift power coefficient (RSC) for the steady state heating (i.e., ψ_{CW}). Then we modulate the laser and repeat the same procedure for the transient-state heating and obtain ψ_{tr}. Having done that, we compute the ratio $\Theta_{exp} = \psi_{tr}/\psi_{CW}$, which relates the average temperature rise under the transient heating to that under the steady-state heating for each ambient temperature condition. However, the temperature rise during measurement is not only a function of the ITR and thermophysical properties, but it strongly depends on the laser absorption coefficient for the sample and the Raman temperature coefficient. While the previous two parameters can be obtained from literature or measured, the uncertainty will increase when incorporated. Here, we utilize the power of ET-Raman to eliminate the effect of the temperature coefficient and absorption coefficient dependency by comparing the steady-state heating to a transient one. In other words, the ratio of ψ_{tr}/ψ_{CW} is calculated to eliminate the dependencies. This work is done repeatedly and systematically at each ambient temperature, starting from 297 K and down to 77 K.

The thermal response of the sample is shown in the schematic diagram in Fig. 2 where the steady state is compared with the transient one, with the thermal diffusion length (L_T) indicated on graph. The distance over which heat diffuses through a material within a specific time interval is effectively infinite for the steady state, and we approximate that as 10 times the diameter of the laser spot. Conversely, the transient state diffusion length is finite and is a function of the thermal diffusivity and the heating time, as $L_T = 2\sqrt{\alpha t_e}$, where α is the thermal diffusivity of the substrate and t_e is the laser pulse width. The value is evaluated to be 130 nm for the SiO$_2$ substrate. To validate our assumption of a negligible temperature rise in the substrate, the conduction thermal resistance must be calculated and compared to the ITR. The conduction thermal resistance can be calculated as $R' = Ln(r_2/r_1)/(2\pi\kappa_s)$ where κ_s is the substrate thermal conductivity taken as 1.2 W·m^{-1}·K^{-1} [29], r_1 is the contact width of the sample with substrate and is taken to be 1 nm, and r_2 is taken to be the thermal diffusion length for the transient state (i.e., 130 nm), and the thickness of the SiO$_2$ for the steady state (i.e., 300 nm). We note that by using the thickness of the SiO$_2$ layer for the steady-state heating calculations, we effectively neglect any thermal resistance that
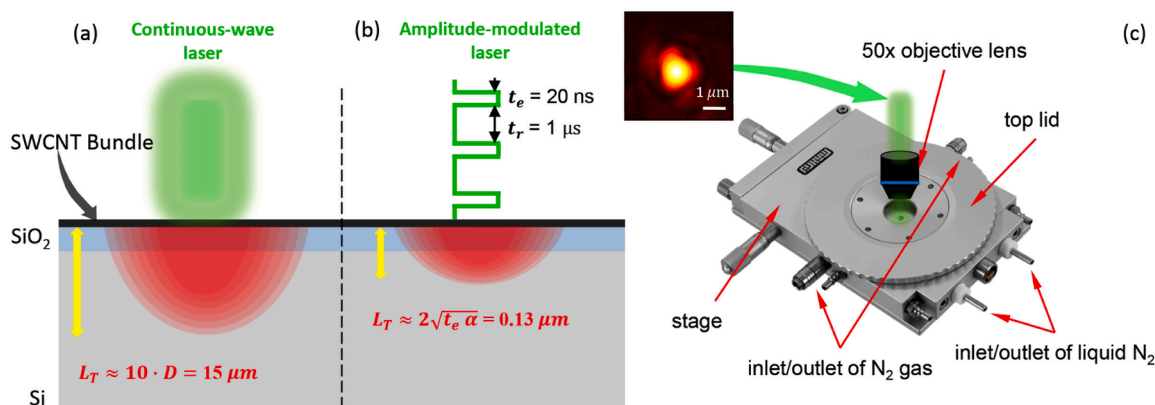

Fig. 2. (a) The steady state energy transport schematic using a continuous-wave (CW) laser with 532 nm wavelength with the thermal diffusion length (L_T) shown in yellow arrow. The steady state diffusion length is practically infinite, but is assumed to be 10 times the laser spot size. (b) The transient energy transport state using an amplitude-modulated CW laser with 532 nm wavelength, with the thermal diffusion length in yellow arrow defined as $L_T = 2\sqrt{\alpha t_e}$, where α is the thermal diffusivity of the substrate, t_e is the heating time which is set to be 20 ns. The relaxation time (t_r) is chosen to be 1 μs to ensure that the sample cools down to room temperature during laser off-time. (c) Cell chamber for cryogenic measurement down to 77 K, with the laser spot shown in the inset.

might arise in the silicon wafer. This is justified since κ of Si is roughly 100 times that of SiO$_2$. By substituting the values, we calculate the substrate thermal resistance in the steady and the transient states to be 0.76 and 0.65 K·m·W^{-1}. They are negligible when compared to the ITR determined experimentally which is found to be of order 10^2 K·m·W^{-1} at room temperature. To sum it up, the ITR governs the heat conduction at the nanoscale, and this justifies our assumption of an isothermal boundary condition on the substrate side (i.e., no temperature rise in the substrate). More details will be provided in the Results and Discussion section.

4. Theoretical model development for heat conduction

The theoretical model for heat conduction is built upon the assumption that heat is transferred by means of conduction only, neglecting the impact of the convection and radiation heat transfer modes. The convection heat transfer coefficient for air at low Reynolds number is of the order $\sim$ 25 W·m^{-2}·K^{-1}. The radiation heat transfer coefficient (h_r) is calculated to be 6.64 W·m^{-2}·K^{-1}. The calculations for h_r will be provided in the Results and Discussion section. These values are 4–5 orders of magnitude lower than the interfacial thermal conductance as calculated in this work and previous ones [1]. Another assumption is implemented by considering an isothermal boundary condition on the substrate side. This has been justified earlier by calculating the conduction thermal resistance and comparing it with the order of magnitude of the ITR. The validity of these assumptions will be discussed in the Results and Discussion section. Under these assumptions, the governing equation for the heat conduction is given as:

$$\kappa \frac{\partial^2 T}{\partial x^2} - \frac{T - T_s}{R \cdot A_c} + \dot{q} = \rho c \frac{\partial T}{\partial t}, \tag{1}$$

where the right-hand side represents the transient response and is set to zero for steady state heating. Here, κ denotes the thermal conductivity of the sample as reported in our recently published work for various temperatures [30], ρ is the density, c the specific heat, T_s the substrate temperature, and A_c the cross-sectional area of the CNT bundle. The second order term in the equation represents the heat conduction along the bundle in the x-direction (axial direction), while the second term represents the heat transfer in the thickness direction (termed "c-axis" hereafter) from SWCNT to the Si substrate, which is governed by the ITR.

The induced laser heating ($\dot{q}$) is represented by a Gaussian profile and is defined as:

$$\dot{q}(x) = \dot{q}_0 \exp\left(-x^2 / r_0^2\right), \tag{2}$$

where $\dot{q}_0$ is the maximum heat source at the laser beam's center ($x = 0$), and r_0 is the laser beam radius, which is measured to be 0.75 μm as shown in Fig. 2.

While the thermal conductivity is borrowed from our recently published work, it can be measured simultaneously with the ITR by controlling the laser spot size. This can be achieved by using different objective lenses in the measurement. A qualitative argument can be constructed as follows: suppose we use a large laser heating spot that covers the entire sample, the heat conduction is then controlled via the interfacial thermal conductance with the substrate in the cross-plane direction, and the in-plane thermal conductivity of the sample will play little to no role in the measured thermal response. On the other hand, if the laser heating size was a point-like source, then the in-plane thermal conductivity will play a more significant role in dictating the thermal transport, whereas the ITR impact will be reduced. By analyzing the thermal response under these two distinct conditions, we can infer the thermal conductivity as well as the ITR simultaneously. We note that the thermophysical properties in Eq. (1) vary drastically with temperature, which has a direct impact on the data processing. To explain the

physics behind such variation, take the specific heat capacity for instance, which to some extent can be explained by the Debye model. At low temperatures, phonons do not get scattered by a single defect due to their long wavelength, and therefore, the effect of a single defect on the transmission function of phonons is almost negligible [31]. However, this behavior changes significantly at high temperatures when shorter wavelength phonons get excited, the transmission function deviates dramatically from the ideal stepwise structure [32]. Further, optical phonons are frozen out at low temperatures, leading to a linear temperature dependence of thermal conductivity, which approaches zero as the temperature approaches absolute zero. This linear relationship is quantized in terms of fundamental constants, with the proportionality constant being $4\pi^2 k_B^2/(3\hbar)$, where the factor 4 represents the four acoustic branches [33]. Notably, this linear temperature slope at low temperatures is independent of the diameter of the tube. As the temperature increases, the contribution of optical phonons to thermal transport becomes increasingly significant, and the thermal conductivity deviates from the linear temperature dependence observed at low temperatures. The range of temperatures at which the thermal conductivity changes linearly with temperature is dependent on the diameter of the tube. Specifically, smaller-diameter tubes require higher temperatures to activate the lowest-energy optical phonon mode, resulting in a higher temperature range needed to deviate from the linear dependence [34]. This phenomenon can be attributed to the increase in the energy gap of the lowest optical phonon as the size of the tube decreases.

Previous research has shown that defects introduced during the synthesis process can compromise CNT's κ. The influence of impurities in low-dimensional structures can be much greater than in bulk materials [35]. In support of this, Maruyama *et al.* [36] have investigated the impact of isotope impurities on CNTs. Their results show a significant decrease of 40 % in CNTs' κ due to impurities. This result highlights the critical role defects and impurities can play in determining the thermal transport properties of CNTs, and in low-dimensional structures in general. We have measured the thermal conductivity variation with temperature for SWCNT bundle in our recent work [30]. The results show a non-monotonic behavior, where it increases at low temperatures and peaks around 200 K, and then starts to decrease. The range of temperatures is similar to the current study, from 77 to 297 K. The explanation for such behavior can be understood by various phonon scattering processes. Namely, the scattering due to various defects in the material, and Umklapp scattering where phonons get scattered by each other. The former is weak temperature dependent or independent and dominates at low temperatures. The latter, however, depends on the phonon population governed by the Boltzmann factor, which itself embodies temperature dependency. As the temperature increases, more phonons get excited leading to more Umklapp scattering events, and therefore, lower thermal conductivity. The specific heat variation with temperature for SWCNT is obtained from Ref. [37]. We feed these temperature-dependent thermophysical properties values to our numerical simulation to capture the impact of temperature variation which yields more accurate results for ITR determination.

It is important to note that the results obtained in the previous section (i.e., $\Theta_{exp} = \psi_{tr}/\psi_{CW}$) represents the average temperature rise of the irradiated region of the sample. Hence, we must account for this by averaging the results in the theoretical model. The steady-state heating, as the name suggests, is time independent and therefore the Raman-intensity weighted average temperature rise can be calculated by integrating over the spatial domain as: $\Delta\overline{T}_{CW} = \int_0^{x_0} I\Delta T \cdot dx / \int_0^{x_0} I \cdot dx$ where I is the intensity that takes the form $I = I_0 \exp\left(-x^2/r_0^2\right)$. On the other hand, the transient state is time dependent, and the temperature rise must be weighted over the temporal and the spatial domains as $\Delta\overline{T}_{tr} = \int_0^{t_0} \int_0^{x_0} I\Delta T \cdot dxdt / \int_0^{t_0} \int_0^{x_0} Idxdt$, where t_0 is the laser pulse width (20 ns). The weighted theoretical temperature rise ratio $\Theta = \Delta\overline{T}_{tr}/\Delta\overline{T}_{CW}$ can be plotted as a function of the ITR (R') at each ambient temperature, which is shown in Fig. 4c for three different ambient temperatures and will be

discussed later. One can clearly notice the different output for the theoretical results with ambient temperatures by comparing the three different curves. This in fact is a manifestation of the impact of temperature on the thermophysical properties, which is involved in heat conduction. The ITR can be determined by interpolating the Θ_{exp} in the $\Theta \sim$ ITR curve.

5. Results and discussion

5.1. Interfacial thermal resistance

Following the experimental procedure described in Section 2, we present some of the results for the first location in Fig. 3. The Raman intensity contour of the G band (~ 1586 cm^{-1}) as a function of the laser power for the transient state and the steady state at 237 K are shown in Fig. 3a and b, respectively. We use the G band for characterizing the sample since it has the highest signal-to-noise ratio, where the redshift can be clearly observed as the laser power increases. The RSC calculated as $\psi_{CW} = \partial\omega/\partial P$ quantifies that redshift and the results are presented in Fig. 3c. The power of ET-Raman can be clearly seen by inspecting the RSC results. First, the RSC depends heavily on the intensity of the collected Raman signal, which itself is a function of the optical focus. For

more reliable results, the focus should be maintained around the same level, which can be hard to meet throughout the whole experiment. However, since ET-Raman technique depends solely on the relative redshift, the effect of being more in-focus or out-of-focus can be also eliminated, providing that the two energy transport state measurements are done successively, which is the case. For instance, the value of RSC at 137 K clearly deviated from the general trend, which we suspect to be due to focus-level discrepancies. Yet, since this observation exist in the two energy states (i.e., the steady and the transient states), they cancel each other, and that abnormality is no longer observed in the ratio Θ_{exp} at 137 K as shown in Fig. 4a. The RSC values in Fig. 3c show little variation up to 200 K, then it starts to increase with increased temperature. The RSC gives an indication about the temperature rise in the sample, the higher the RSC, the higher the temperature rise. We interpret this as a possible increase of the overall thermal resistance as the thermal conductivity decreases where it starts to drop around 200 K as mentioned earlier. It is worth noting that the RSC information can be greatly affected by the optical focus of the laser. Therefore, the ratio $\Theta_{exp} = \psi_{tr}/\psi_{CW}$ provides more reliable insights.

The average temperature rise of the sample can be obtained by referring to Fig. 3d which illustrates the Raman spectrum variation with temperature. It is evident that at higher temperatures the Raman-active
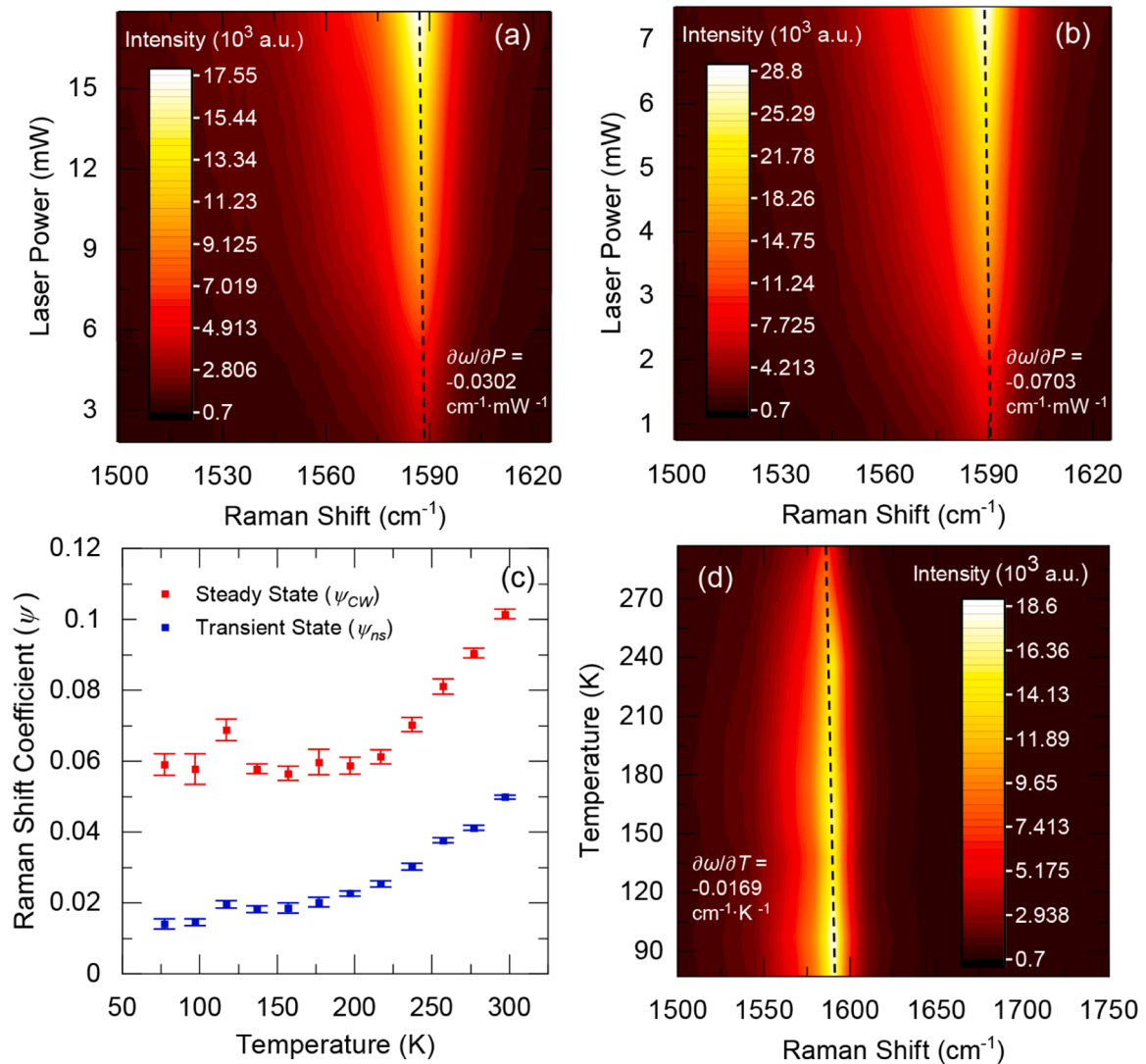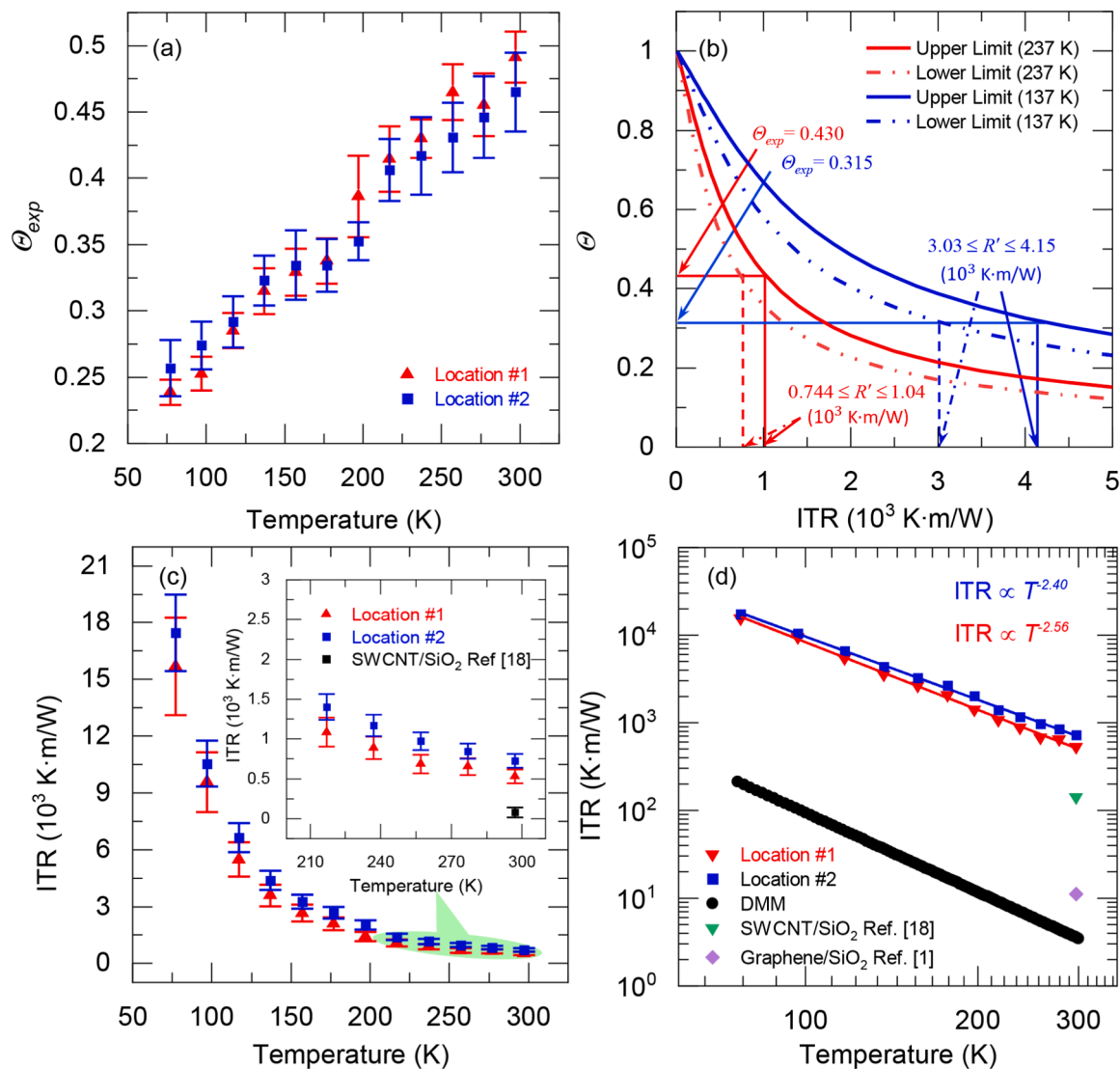

Fig. 3. A 2D contour for Raman shift variation with laser power at Location #1 at 237 K for (a) transient state and (b) steady state. (c) Raman shift coefficient variation with temperature for the two energy transport states. (d) 2D contour for Raman shift variation with temperature, with the Raman temperature coefficient shown in the figure.

Fig. 4. (a) The experimental Raman shift power coefficient ratio's (Θ_{exp}) variation with temperature. (b) The theoretical temperature rise ratio of the first location as a function of ITR at two different temperatures. The solid and dashed lines set the upper and lower limits of the ITR, respectively. The measured Θ_{exp} are mapped onto the graph to extract the ITR. (c) The determined ITR values as a function of temperature for the two locations. The inset shows trend details and uncertainties at high temperatures. (d) The ITR~T trend showing the T^{-n} relation compared with DMM calculations with a T^{-3} law.

G-band undergoes a redshift, consistent with previous observations found in the literatures. The Raman temperature coefficient ($\partial\omega/\partial T$) can be determined by fitting the peaks' location against the temperature which yields a value of -0.0169 cm$^{-1}\cdot$K^{-1}. This value is within the range for different carbon-based materials. Namely, -0.011 cm$^{-1}\cdot$K^{-1} for highly oriented pyrolytic graphite, -0.028 cm$^{-1}\cdot$K^{-1} for disordered graphite [38], and -0.028 cm$^{-1}\cdot$K^{-1} for MWCNT. Using the RSC and the Raman temperature coefficient, one can estimate the average temperature rise as $\Delta T=(\partial\omega/\partial T)/\partial\omega/\partial P)\cdot\Delta P$, where ΔP is the laser power range used during the experiment. Using the values for the first location at 237 K, we obtain an average temperature rise of 30 °C. This value also represents the temperature difference between the sample and the ambient air, which for a convection heat transfer coefficient of the order ~ 25 W$\cdot$m$^{-2}\cdot$K^{-1} contributes an insignificant amount to the total heat transfer from the sample. This justifies neglecting the heat transfer via convection as stated earlier. On the other hand the radiation heat transfer coefficient can be calculated as $h_r = \sigma(T_2^2 + T_1^2)(T_2 + T_1)$ where σ is the Stefan-Boltzmann constant ($\sigma = 5.67 \times 10^{-8}$ W$\cdot$m$^{-2}\cdot$K^{-4}) T_1 is the substrate temperature which is taken to be room temperature and $T_2 = T_1 + \Delta T$. The value for h_r is determined to be 6.64 W$\cdot$m$^{-2}\cdot$K^{-1}, which

also justifies neglecting it.

The numerical calculation results shown in Fig. 4b for two different temperatures reflect the impact of the variation of thermophysical properties of SWCNTs with temperature. The temperature dependent heat capacity and thermal conductivity is used to capture these effects. We further solve the heat conduction equation twice at each temperature to account for the uncertainty of the effective density. The maximum packing density calculations leads to a higher thermal mass which yields a lower ITR. We map out the experimental temperature rise ratio Θ_{exp} onto the graph to determine the ITR bounds at each temperature. The reported results shown in Fig. 4c are the average of the two bounds at each temperature, with half the difference to quantify the uncertainty. It is observed that the ITR decreases with increased temperature, agreeing with the ones reported earlier for various solid-solid interfaces. The value of the ITR at room temperature is 530 and 725 K$\cdot$m$\cdot$W^{-1} for the first and second locations. These are of similar order of magnitude as the results reported by Shi *et al.* [18] for 1.2 nm metallic SWCNT on SiO$_2$ shown on Fig. 4c. In their work, a joule heating method was used, and the ITR was estimated to be in the range of 17–142 K$\cdot$m$\cdot$W^{-1} at room temperature. We note that their model to deduce the

ITR is sensitive to the thermal conductivity of the SWCNT which is obtained for an assumed value in the range 1000–3000 W·m^{-1}·K^{-1}. This range is much higher than the recently reported one in our lab for SWCNTs of 50 W·m^{-1}·K^{-1} and is used in this study, which could explain the differences in the reported ITR. We note that the thermal conductivity is a strong function of the defects' concentration in the sample, as well as the size of tube as theoretically investigated by Zhang *et al.* using molecular dynamics simulations [39]. Jia *et al.* [40] experimentally measured the thermal conductivity of MWCNT to be around 100 W·m^{-1}·K^{-1}, which is the same order as the one used in the current study.

To have a sense of the order of magnitude of the interfacial thermal conductance (*G*) per unit area, here we assume a contact width of ~1 nm, and obtain *G* as illustrated in Fig. 5a. The current results are compared with the those of a 2.8 nm thick graphene layer on SiO$_2$ reported by Chen *et al.* [1]. Their results ranged from 30 to 95 MW·m^{-2}·K^{-1}, an order of magnitude higher than the reported ones in this work. At low temperatures, the results follow the same trend: increasing with increased temperature. However, at higher temperatures, their reported values seem to become saturated, whereas our results exhibit a monotonic increase up to room temperature. At room temperature, their reported *G* (95 MW/m^2·K) is significantly higher than the current work (1.8 MW·m^{-2}·K^{-1}). We find our values consistent with

the previously reported *G* by Yu *et al.* [41] for carbon nanofibers on silicon where it is measured to be 1.4 MW·m^{-2}·K^{-1}. Schmidt *et al.* [42] reported *G* of 5 MW·m^{-2}·K^{-1} for highly ordered pyrolytic graphite on aluminum at 300 K using the pump-probe thermoreflectance technique. Liu *et al.* [43] investigated the thermal transport across graphene/diamond interface by non-equilibrium molecular dynamics simulations for different numbers of graphene layers. The reported *G* is in the range 18–50 MW·m^{-2}·K^{-1} for 1–6 layers of graphene. The discrepancies in the reported values are likely due to the unique interface structure as well as the different measurement techniques used. Since *G* is known to be a function of temperature, the induced temperature rise during the experiment can play a role in determining *G*. In our experiment, the average temperature rise of 30 K as discussed earlier.

We further calculate the ITR using the diffuse mismatch model (DMM) which accounts for the scattering of phonons at the interface and compare it to our experimental ones. The ITR can be calculated as $R'' = \left[(\pi/15)(k_B^4/\hbar^3) \sum_j v_{i,j}^{-2} \overline{\alpha}_i(\omega) \right]^{-1} T^{-3}$ where k_B is the Boltzmann constant, $\hbar$ is the reduced Planck constant, and $\overline{\alpha}_i(\omega)$ is the averaged transmission probability of the phonons from one side to the other one

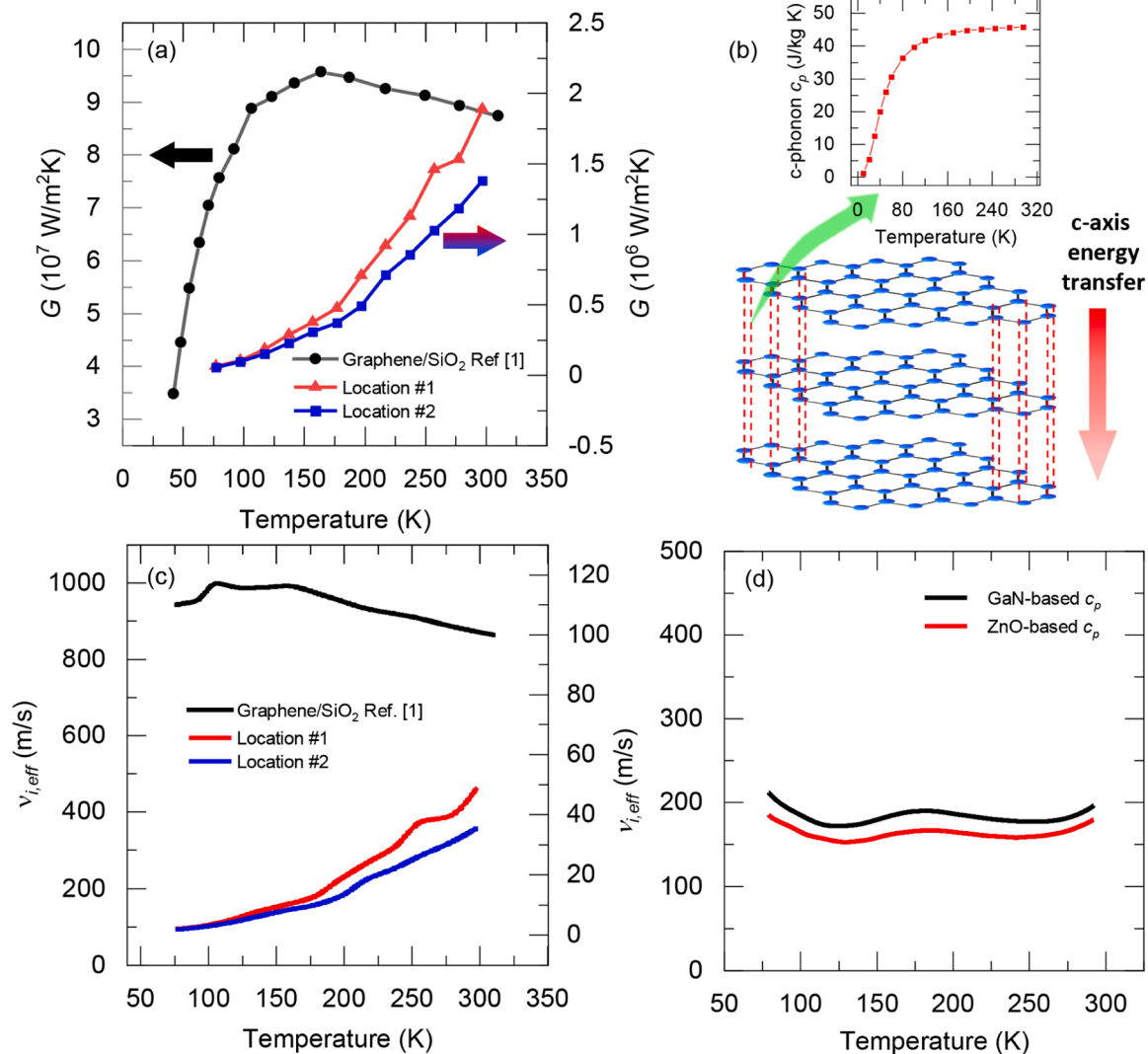**Fig. 5.** (a) The interfacial thermal conductance assuming a contact width of 1 nm with the substrate for this work and Ref. [1]. (b) Schematic of the energy transport in the c-axis with the c-phonon specific heat. The effective energy transmission velocity of the energy carriers at the interface ($v_{i,eff}$) which is defined as the ratio of the interfacial thermal conductance to the volumetric heat capacity for (c) our work and Graphene/SiO$_2$ interface [1], and (d) GaN/ZnO interface [2].

(i=1, 2). Here, i still denotes the side of the interface and goes from 1 to 2, j denotes the phonon mode, which are restricted to the acoustic modes at each side, and v is the phonon group velocity from the literature. The transmission coefficient $\alpha_i(\omega)$ is effectively calculated by the mismatch in the density of states for the two materials across the interface. We utilize the Debye approximation for the density of states and the linear dispersion assumption, and use the reported phonon group velocities for SWCNT [44] and SiO$_2$ [45] which reduce $\overline{\alpha}_i(\omega)$ to take the following form: $\overline{\alpha}_i(\omega) = (1/2)\sum_j v_{3-i,j}^{-2} / \sum_{ij} v_{i,j}^{-2}$.

We make one further simplification by considering the out-of-plane acoustic branch as the mechanism to transfer heat (e.g. the c-axis phonons of graphite). Further discussion in sufficient detail will follow shortly. The DMM calculations provide values for the ITR in K·m^2·W^{-1}, we assume a contact width of ~1 nm to obtain an ITR per unit length for comparison purposes as shown in Fig. 4d. Note this "1 nm" width is just assumed for order estimation, rather than precise calculation. It is evident that the Debye approximation (i.e., the linear dispersion) underestimates the ITR value in the DMM calculations. This is consistent with previous observations made by Duda *et al.* [46] where they demonstrated that the Debye dispersion leads to substantially higher interfacial thermal conductance (underestimated ITR). In our preceding work [20], we reported an ITR value at room temperature of 3000 K·m·W^{-1} for the SWCNT/Si interface. By implementing a qualitative theoretical model, we demonstrated that the presence of an air gap significantly contributes to this ITR. In contrast, the current study has revealed a substantially reduced ITR, ranging between 530 and 725 K·m·W^{-1}. This represents nearly a 75 % decrease from the previously reported value. Such notable reduction hints at a superior contact quality between the sample and substrate in the present investigation. As a result, the conduction via air molecules contributes very little to the heat transport in the current work. A perfect contact is unlikely to exist for van der Waals bonded interfaces. Hence, it will ultimately contribute to the discrepancies between the measured values and the predicted ones. Also for the DMM prediction, we assume a contact width of 1 nm, which could overestimate the contact width for a bundle of only few nm diameter, thereby leading to a lower ITR prediction. Yet, the ITR trend with temperature qualitatively aligns well with the DMM trend, especially when viewed under the log coordinate of ITR. For the experimental results, the ITR-*T* relation can be fitted nicely following a T^{-n} law with n=2.56 and 2.40 for the first and second locations. In calculating ITR by the DMM formulation, the T^{-3} is completely analogous to the Debye T^3 law of specific heat. However, numerous research suggest that the specific heat of graphite can exhibit ~ T^2 dependency after some threshold temperature identified to be 10 K for graphite [47], which we speculate to be the case in our SWCNT sample. Previous work by Chen [48] suggests that in the diffuse limit, the ITR can indeed be calculated as $R'' = 4/(T_{d12}C_1v_1)$ where C is the volumetric heat capacity and v is the phonon group velocity. As can be seen, the ITR is inversely proportional to the heat capacity which can also confirm the observed trend in our experimental results. Our ITR-T trend suggests the Debye temperature of the phonons sustained by the van der Waals interactions between SWCNT and SiO$_2$ should be much higher than 300 K.

5.2. Effective energy transmission velocity at the interface

It is well known that heat can be mediated across the interface via phonons and electrons. As far as graphite is concerned, the energy transport across different carbon layers in the c-axis is dominated by low-frequency phonons, termed c-phonons. This has been demonstrated in our previous work [49] where the different carbon layers exchange the energy via weak van der Waals phonons as shown in Fig. 5b. We have suggested earlier a two-step process in which the interactions across acoustic phonon modes govern the heat conduction along the c-axis [49]. We introduce the concept of anisotropic phonon heat capacity, delineated as C_1 and C_2. While C_1 signifies the volumetric heat

capacity attributed to phonons participating in cross-plane atomic interactions, termed c-phonon heat capacity shown in Fig. 5b, it is noteworthy that C_1 is scalar in nature. Conversely, C_2, termed a-phonon heat capacity, characterizes the volumetric heat capacity of phonons engaged in-plane atomic interactions. In this context, a-phonons convey their energy to c-phonons via in-plane atomic interactions within the same layer, then c-phonons transfer the energy across the SWCNT-SiO$_2$ interface via the van der Waals interaction.

In previous work, Chen [48] has developed a theoretical model for the ITR based on the Boltzmann transport equation (BTE) and the results were in good agreement with numerical solutions of the BTE. Due to the inevitable presence of surface roughness at the interface which can extend from 3 to 9 Å [50], we consider the diffuse scattering limit for phonons. As mentioned earlier, the ITR can then be calculated using $R'' = 4/(T_{d12}C_1v_1)$ [48], where T_{d12} is the phonon transmissivity at the interface and can be calculated as $T_{dij} = C_jv_j/(C_iv_i + C_jv_j)$ [5], C is the volumetric heat capacity and v the phonon group velocity, which can be obtained from dispersion relations. The indices "i" and "j" denote the side of the interface. Under this formulation, the transmission probability T_{d12} (i.e., from side 1 to side 2) is not equal to T_{d21}. Under these conditions, it can be clearly seen that we must deal with the inescapable probabilistic nature of phonon transmission.

To subtract the impact of heat capacity on ITC variation with temperature, we introduce a parameter termed effective energy transmission velocity across the interface ("$v_{i,eff}$" hereafter), which is defined as $v_{i,eff} = G/\rho c_p$. By considering c-phonons only as the way to mediate the energy in the cross-plane, the results for the interfacial thermal conductance shown in Fig. 5a are divided by C_1 (c-phonon specific heat) to obtain $v_{i,eff}$ for our sample. The results are compared with the one obtained from Chen *et al.* [1] for graphene (Fig. 5c). In this work, $v_{i,eff}$ varies from 1 to 60 m/s for the two locations as shown in Fig. 5c. We observe that $v_{i,eff}$ is an order of magnitude lower than the one obtained for Chen *et al.*'s work [1], which held almost constant around 900 m/s. We explore the $v_{i,eff}$ for various interfaces found in literatures and observe an almost constant value that varies little for a wide range of temperatures and is more apparent at high temperatures. For instance, for metallic interfaces, such as Al-Cu [14], we find $v_{i,eff}$ to be an order of magnitude lower than the Fermi velocity. For interfaces where the heat conduction is dominated by phonons, as the one shown in Fig. 5d for GaN/ZnO [2], $v_{i,eff}$ is an order of magnitude lower than that of the acoustic phonon branches. Since $v_{i,eff}$ depends on ρc_p used in the calculation, we process the data based on ρc_p for ZnO and GaN and compare the results. As shown in Fig. 5d, the results are quite similar, where $v_{i,eff}$ is found to be in the range of 150–200 m/s. We find the lower $v_{i,eff}$ when compared to energy carrier velocities (Fermi velocity, phonon group velocity) is consistent with previous formulation to the ITR as adopted from literatures [5,48]. The range of velocities obtained in this work are in line when applying the ITR approximation using the formula $R'' = 4/(T_{d12}C_1v_1)$ for diffuse scattering conditions and suggests an average transmission coefficient of ~10 %. For the largely varying $v_{i,eff}$ for our results, we speculate the C_1 used in the calculation does not represent that of the local van der Waals bonds.

At the interface, the cross-plane atomic interactions directly lead to the *c*-axis heat conduction, facilitating direct energy exchange among phonons through these interactions. The term "*c*-phonon" encompasses all phonon modes arising from atomic interactions along the *c*-axis. The specific heat used in the above analysis is for c-phonons of graphite. For a SWCNT bundle on Si, c-phonons will have different dispersion relations and specific heat since the C-Si van der Waals bond is different from the C—C van der Waals bond in graphite. However, this uncertainty will only impact the newly introduced concept $v_{i,eff}$ which is still under exploration and will be refined in our future work. In summary, we expect this parameter to give an intrinsic picture of the transmission of heat carriers, not related to the temperatre-dependent heat capacity. The primary origin of ITR as in the AMM and DMM is phonon reflection

at the interface. By assuming a constant group velocity for phonons as adopted in the Debye model, one can indicate how the average phonon transmission coefficient changes with temperature. Thus, we conclude that in several cases, the transmission probability is unaltered and remains constant. Hence, by observing a non-constant $v_{i,eff}$, it is very likely that inelastic phonon transmission plays a significant role in the heat transport. This is the case for interfaces of solids with dissimilar Debye temperatures. Future research efforts are directed to make practical use of such observations.

6. Conclusion

In this work we systematically investigated the impact of temperature on the energy coupling across SWCNT bundle/SiO$_2$ interface at two locations with bundle heights of 7.7 and 5.55 nm. The ET-Raman technique used in this work ensures sound measurement accuracy as the laser absorption data and sample temperature rise is not needed. The ITR was measured from 297 K down to 77 K, where it has increased over an order of magnitude. This strong temperature dependency is found to follow a T^{-n} law where n is 2.56 and 2.4 for the first and second locations, respectively. At room temperature, the measured ITR of 530–725 K·m·W^{-1} are close to that of SWCNT/SiO$_2$ interface in the literature. We further compared our ITR results with the ones predicted by the DMM model and observed a great qualitative agreement, despite that the DMM calculations being significantly less in magnitude. These discrepancies are consistent with previous reported work where the DMM under the Debye approximation of linear dispersion massively underestimates the ITR. A new concept termed interface effective energy transmission velocity ($v_{i,eff}$) was introduced, which relates G to the volumetric heat capacity. We observed an almost unaltered $v_{i,eff}$ as the temperature changes for various interfaces. Depending on the nature of the interface, we observed an order of magnitude lower $v_{i,eff}$ than the Fermi and acoustic phonon group velocities for metallic and semiconducting interfaces. Further refinement of this concept will be considered in future work. While this work has considered a ~ 8 nm width bundle, future research efforts will be directed towards pushing the limit to ~ 1 nm individual SWCNT. Despite the great challenge, advancements in growth and nanofabrication techniques make the sample preparation achievable. A greater challenge arises from the low scattering volume of individual SWCNT and therefore a weaker Raman signal. Hence, we anticipate that ET-Raman should be replaced by the frequency-domain energy transport state-resolved Raman (FET-Raman) which provides stronger signal and feasible probing.

CRediT authorship contribution statement

Ibrahim Al Keyyam: Writing – original draft, Investigation, Formal analysis, Data curation, Conceptualization. **Mahya Rahbar:** Writing – review & editing, Investigation, Formal analysis, Data curation. **Nicholas Hunter:** Writing – review & editing, Methodology, Formal analysis, Data curation. **Baini Li:** Writing – review & editing, Resources, Data curation. **Tianyu Wang:** Writing – review & editing, Methodology, Investigation, Formal analysis, Data curation, Conceptualization. **Enzheng Shi:** Writing – review & editing, Project administration, Investigation, Formal analysis, Conceptualization. **Xinwei Wang:** Writing – review & editing, Supervision, Software, Resources, Project administration, Methodology, Investigation, Funding acquisition, Formal analysis, Data curation, Conceptualization.

Declaration of competing interest

The authors declare that they have no known competing financial interests or personal relationships that could have appeared to influence the work reported in this paper.

Data availability

Data will be made available on request.

References

[1] Z. Chen, W. Jang, W. Bao, C.N. Lau, C. Dames, Thermal contact resistance between graphene and silicon dioxide, Appl. Phys. Lett. 95 (16) (2009) 161910.

[2] J.T. Gaskins, G. Kotsonis, A. Giri, S. Ju, A. Rohskopf, Y. Wang, T. Bai, E. Sachet, C. T. Shelton, Z. Liu, Z. Cheng, B.M. Foley, S. Graham, T. Luo, A. Henry, M.S. Goorsky, J. Shiomi, J.P. Maria, P.E. Hopkins, Thermal boundary conductance across heteroepitaxial ZnO/GaN interfaces: assessment of the phonon gas model, Nano Lett. 18 (12) (2018) 7469–7477.

[3] X. Feng, D. Ren, X. He, M. Ouyang, Mitigating thermal runaway of lithium-ion batteries, Joule 4 (4) (2020) 743–770.

[4] W.A. Little, The transport of heat between dissimilar solids at low temperatures, Can. J. Phys. 37 (3) (1959) 334–349.

[5] E.T. Swartz, R.O. Pohl, Thermal Boundary Resistance, Rev. Mod. Phys. 61 (3) (1989) 605–668.

[6] J. Zhang, Y. Wang, X. Wang, Rough contact is not always bad for interfacial energy coupling, Nanoscale 5 (23) (2013) 11598–11603.

[7] M.A. Osman, T. Kim, M.J. Schulz, V. Shanov, Z. Yin, M. Cahay, Chapter 24 - thermal interface resistance between silicon and single wall carbon nanotubes. Nanotube Superfiber Materials, 2nd ed., William Andrew Publishing, 2019, pp. 603–621.

[8] Y. Feng, J. Zhu, D. Tang, Effect of van der Waals forces on thermal conductance at the interface of a single-wall carbon nanotube array and silicon, AIP. Adv. 4 (12) (2014) 127118.

[9] E.C.J. Ng, M.V. Tran, Y.M. Hung, Thermal resistance analysis of micro heat pipes incorporated with carbon nanotubes nanocapillaries, Int. J. Heat. Mass Transf. 216 (2023) 124611.

[10] R. Xiang, Atomic precision manufacturing of carbon nanotube—A perspective, Int. J. Extreme Manuf. 4 (2) (2022) 023001.

[11] X. Guo, S. Cheng, W. Cai, Y. Zhang, X.a. Zhang, A review of carbon-based thermal interface materials: mechanism, thermal measurements and thermal properties, Mater. Des. 209 (2021) 109936.

[12] E. Pop, Energy dissipation and transport in nanoscale devices, Nano Res. 3 (3) (2010) 147–169.

[13] K. Razeeb, E. Dalton, G. Cross, A. Robinson, Present and future thermal interface materials for electronic devices, Int. Mater. Rev. 63 (2017) 1–21.

[14] B.C. Gundrum, D.G. Cahill, R.S. Averback, Thermal conductance of metal-metal interfaces, Phys. Rev. B 72 (24) (2005) 245426.

[15] G.D. Mahan, M. Bartkowiak, Wiedemann–Franz law at boundaries, Appl. Phys. Lett. 74 (7) (1999) 953–954.

[16] E. Pop, D.A. Mann, K.E. Goodson, H. Dai, Electrical and thermal transport in metallic single-wall carbon nanotubes on insulating substrates, J. Appl. Phys. 101 (9) (2007) 093710.

[17] H. Maune, H.Y. Chiu, M. Bockrath, Thermal resistance of the nanoscale constrictions between carbon nanotubes and solid substrates, Appl. Phys. Lett. 89 (1) (2006) 013109.

[18] L. Shi, J. Zhou, P. Kim, A. Bachtold, A. Majumdar, P.L. McEuen, Thermal probing of energy dissipation in current-carrying carbon nanotubes, J. Appl. Phys. 105 (10) (2009) 104306.

[19] J. Yang, S. Waltermire, Y. Chen, A.A. Zinn, T.T. Xu, D. Li, Contact thermal resistance between individual multiwall carbon nanotubes, Appl. Phys. Lett. 96 (2) (2010) 023109.

[20] I. Al Keyyam, M. Rahbar, E. Shi, B. Li, T. Wang, X. Wang, Thermal Conductance between <6nm Single-Walled Carbon Nanotube Bundle and Si Substrate, J. Phys. Chem. C (2024) 1505–1517.

[21] T. Wang, R. Wang, P. Yuan, S. Xu, J. Liu, X. Wang, Interfacial Thermal Conductance between Mechanically Exfoliated Black Phosphorus and SiO$_x$: effect of Thickness and Temperature, Adv. Mater. Interfaces. 4 (16) (2017) 1700233.

[22] A. Taube, J. Judek, A. Łapińska, M. Zdrojek, Temperature-Dependent Thermal Properties of Supported MoS$_2$ Monolayers, ACS. Appl. Mater. Interfaces. 7 (9) (2015) 5061–5065.

[23] J. Liu, I. Al Keyyam, Y. Xie, X. Wang, Perspectives on interfacial thermal resistance of 2D materials: raman characterization and underlying physics, Surf. Sci. Technol. 2 (1) (2024) 8.

[24] H. Zobeiri, N. Hunter, S. Xu, Y. Xie, X. Wang, Robust and high-sensitivity thermal probing at the nanoscale based on resonance Raman ratio (R3), Int J Extreme Manuf 4 (3) (2022) 035201.

[25] J. Hou, X. Wang, P. Vellelacheruvu, J. Guo, C. Liu, H.M. Cheng, Thermal characterization of single-wall carbon nanotube bundles using the self-heating 3ω technique, J. Appl. Phys. 100 (12) (2006) 124314.

[26] C. Li, S. Xu, Y. Yue, B. Yang, X. Wang, Thermal characterization of carbon nanotube fiber by time-domain differential Raman, Carbon. N. Y. 103 (2016) 101–108.

[27] A.T. Winzer, C. Kraft, S. Bhushan, V. Stepanenko, I. Tessmer, Correcting for AFM Tip Induced Topography Convolutions in Protein–DNA Samples, Ultramicroscopy. 121 (2012) 8–15.

[28] R. Wang, T. Wang, H. Zobeiri, P. Yuan, C. Deng, Y. Yue, S. Xu, X. Wang, Measurement of the thermal conductivities of suspended MoS$_2$ and MoSe$_2$ by nanosecond ET-Raman without temperature calibration and laser absorption evaluation, Nanoscale 10 (48) (2018) 23087–23102.

[29] W. Zhu, G. Zheng, S. Cao, H. He, Thermal conductivity of amorphous SiO$_2$ thin film: a molecular dynamics study, Sci. Rep. 8 (1) (2018) 10537.

[30] M. Rahbar, B. Li, N. Hunter, I. Al Keyyam, T. Wang, E. Shi, X. Wang, Observing grain boundary-induced phonons mean free path in highly aligned SWCNT bundles by low-momentum phonon scattering, Cell Reports Physical Science (2023) 101688.

[31] T. Yamamoto, S. Watanabe, K. Watanabe, Universal features of quantized thermal conductance of carbon nanotubes, Phys. Rev. Lett. 92 (7) (2004) 075502.

[32] L.G.C. Rego, G. Kirczenow, Quantized thermal conductance of dielectric quantum wires, Phys. Rev. Lett. 81 (1) (1998) 232–235.

[33] H.Y. Chiu, V.V. Deshpande, H.W.C. Postma, C.N. Lau, C. Mikó, L. Forró, M. Bockrath, Ballistic phonon thermal transport in multiwalled carbon nanotubes, Phys. Rev. Lett. 95 (22) (2005) 226101.

[34] J. Hone, M.C. Llaguno, M.J. Biercuk, A.T. Johnson, B. Batlogg, Z. Benes, J. E. Fischer, Thermal properties of carbon nanotubes and nanotube-based materials, Appl. Phys. A Mater. Sci. Process. 74 (3) (2002) 339–343.

[35] N. Kondo, T. Yamamoto, K. Watanabe, Molecular-dynamics simulations of thermal transport in carbon nanotubes with structural defects, E-J. Surf. Sci. Nanotechnol. 4 (0) (2006) 239–243.

[36] S. Maruyama, Y. Igarashi, Y. Taniguchi, J. Shiomi, Anisotropic Heat Transfer of Single-Walled Carbon Nanotubes, J. Therml. Sci. Technol. 1 (2) (2006) 138–148.

[37] J. Hone, B. Batlogg, Z. Benes, A.T. Johnson, J.E. Fischer, Quantized Phonon Spectrum of Single-Wall Carbon Nanotubes, Science 289 (5485) (2000) 1730–1733.

[38] P. Tan, Y. Tang, Y.M. Deng, F. Li, Y.L. Wei, H.M. Cheng, Resonantly enhanced Raman scattering and high-order Raman spectra of single-walled carbon nanotubes, Appl. Phys. Lett. 75 (11) (1999) 1524–1526.

[39] Y. Zhang, A. Fan, M. An, W. Ma, X. Zhang, Thermal transport characteristics of supported carbon nanotube: molecular dynamics simulation and theoretical analysis, Int. J. Heat. Mass Transf. 159 (2020) 120111.

[40] Q. Jia, Y. Zhou, X. Li, L. Lindsay, L. Shi, Differential multi-probe thermal transport measurements of multi-walled carbon nanotubes grown by chemical vapor deposition, Int. J. Heat. Mass Transf. 216 (2023) 124535.

[41] C. Yu, S. Saha, J. Zhou, L. Shi, A.M. Cassell, B.A. Cruden, Q. Ngo, J. Li, Thermal contact resistance and thermal conductivity of a carbon nanofiber, J. Heat. Transfer. 128 (3) (2005) 234–239.

[42] A.J. Schmidt, X. Chen, G. Chen, Pulse accumulation, radial heat conduction, and anisotropic thermal conductivity in pump-probe transient thermoreflectance, Rev. Scient. Instrum. 79 (11) (2008) 114902.

[43] Y. Liu, L. Qiu, J. Liu, Y. Feng, Enhancing thermal transport across diamond/graphene heterostructure interface, Int. J. Heat. Mass Transf. 209 (2023) 124123.

[44] M.S. Dresselhaus, P.C. Eklund, Phonons in carbon nanotubes, Adv. Phys. 49 (6) (2000) 705–814.

[45] D. Brick, E. Emre, M. Grossmann, T. Dekorsy, M. Hettich, Picosecond photoacoustic metrology of SiO$_2$ and LiNbO$_3$ layer systems used for high frequency surface-acoustic-wave filters, Appl Sci 7 (8) (2017) 822.

[46] J.C. Duda, T.E. Beechem, J.L. Smoyer, P.M. Norris, P.E. Hopkins, Role of dispersion on phononic thermal boundary conductance, J. Appl. Phys. 108 (7) (2010) 073515.

[47] Y. Xie, Z. Xu, S. Xu, Z. Cheng, N. Hashemi, C. Deng, X. Wang, The defect level and ideal thermal conductivity of graphene uncovered by residual thermal reffusivity at the 0K limit, Nanoscale 7 (22) (2015) 10101–10110.

[48] G. Chen, Thermal conductivity and ballistic-phonon transport in the cross-plane direction of superlattices, Phys. Rev. B 57 (23) (1998) 14958.

[49] M. Han, J. Liu, Y. Xie, X. Wang, Sub-μm c-axis structural domain size of graphene paper uncovered by low-momentum phonon scattering, Carbon. N. Y. 126 (2018) 532–543.

[50] G. Chen, M. Neagu, Thermal conductivity and heat transfer in superlattices, Appl. Phys. Lett. 71 (19) (1997) 2761–2763.